frontiers | Frontiers in Materials

TYPE Original Research
PUBLISHED 20 November 2025
DOI 10.3389/fmats.2025.1713051

OPEN ACCESS

EDITED BY
Liang Zhang,
Xiamen University of Technology, China

REVIEWED BY
Pavlo Maruschak,
Ternopil Ivan Pului National Technical University, Ukraine
Luyang Xu,
North Dakota State University, United States

*CORRESPONDENCE
Xingyu Zhu,
470280612@qq.com

RECEIVED 25 September 2025
REVISED 25 October 2025
ACCEPTED 03 November 2025
PUBLISHED 20 November 2025

CITATION
Li J, Shen J, Tan L, Zhang L, Du D, Liao Y and Zhu X (2025) Numerical study of corrosion in high pressure vent pipelines at high sulfur natural gas stations considering liquid phase accumulation and erosion.
Front. Mater. 12:1713051.
doi: 10.3389/fmats.2025.1713051

Numerical study of corrosion in high pressure vent pipelines at high sulfur natural gas stations considering liquid phase accumulation and erosion

Jing Li[1], Jun Shen[1], Longhua Tan[2], Liang Zhang[1], Defei Du[2], Yihong Liao[3] and Xingyu Zhu[3]*

[1]Safety, Environment and Technology Supervision Research Institute, PetroChina Southwest Oil and Gasfield Company, Chengdu, China, [2]PetroChina Southwest Oil and Gasfield Company, Chengdu, China, [3]School of Petroleum and Gas Engineering, Southwest Petroleum University, Chengdu, China

In high-sulfur natural gas stations, vent pipelines, especially at their elbows, experience acidic corrosion and erosion, which affects the safety of the pipelines. On-site wall thickness measurements of pipelines are empirical and random, failing to provide a comprehensive and accurate reflection of the corrosion status of the entire vent pipeline. This study used computational fluid dynamics (CFD) to simulate an actual high-pressure vent pipeline. By analyzing the flow field distribution, the location of liquid phase accumulation was determined, and the areas of severe erosion were identified. This information can provide a basis for selecting reasonable corrosion measurement points on-site.

KEYWORDS

CFD simulation, liquid phase accumulation, erosion, vent pipeline, high-sulfur natural gas station

1 Introduction

The vent pipeline is an indispensable component of natural gas stations, with its primary function being to discharge substances that may jeopardize the normal operation and maintenance of the pipeline, thereby ensuring the stable and safe operation of the natural gas station. However, the corrosion issue in vent pipelines, particularly those in high-sulfur natural gas stations, has become a critical factor affecting their safety and reliability. High-sulfur natural gas contains a large amount of hydrogen sulfide (H_2S), and in the presence of liquid water, vent pipelines face two main corrosion mechanisms: acidic corrosion and droplet erosion (Zhao et al., 2016; Xu et al., 2017; Fujisawa et al., 2015). Acidic corrosion arises from the reaction of hydrogen sulfide with liquid water to produce acidic substances, leading to chemical corrosion of metal materials; droplet erosion stems from gas flow carrying droplets that impact the inner surface of the pipeline during venting, causing surface wear. Both mechanisms result in wall thickness reduction, thereby shortening the service life and threatening overall safety.

To safeguard the vent pipelines, regular wall thickness measurements are typically required. When selecting measurement points, on-site personnel often rely on experience to choose corrosion-prone areas, such as elbows, tees, and reducers, which are more susceptible to corrosion due to changes in fluid flow direction. However, this empirical method lacks

systematic theoretical support. Additionally, vent pipelines are frequently installed at high elevations with small diameters, making on-site inspections operationally challenging; some buried pipelines also have detection blind spots. Therefore, on-site measurement methods have limitations and cannot comprehensively or accurately assess the corrosion condition of the entire vent pipeline.

To overcome these challenges, researchers in recent years have developed various methods for predicting internal corrosion, primarily focusing on identifying locations of liquid water accumulation and erosion. A literature review indicates that significant progress has been made in using computational fluid dynamics (CFD) to predict corrosion in general pipelines, especially in natural gas transportation pipelines. For example (Hu and Cheng, 2016), employed CFD simulations to analyze the distribution of water phase volume fraction and wall shear stress in two-phase fluid flows, thereby identifying water accumulation zones and determining potential corrosion areas (Chen et al., 2017). Explored the droplet carrying mechanisms and liquid accumulation formation in engineering pipeline transportation processes, verifying a good match between predicted corrosion locations and actual corrosion points(Fujisawa et al., 2016). Constructed a numerical method combining Euler/Lagrange CFD models with erosion models to evaluate the effects of factors such as droplet velocity, diameter, number density, impact angle, material hardness, liquid film thickness, and erosion depth on wall thinning rates (Hong et al., 2021). Investigated erosion patterns in structures like rectangular pipes and tees, finding that erosion is most intense at the blind end of blind tee pipes. In addition, Maruschak et al. (2016) explored visual assessment and classification methods for corrosion defects to support corrosion prediction and management.

Further research has extended the application of CFD in predicting erosion-corrosion in pipeline elbows and bends under multiphase flows. For instance, Darihaki et al. (2021) developed a CFD method that considers particle sizes near the wall and evaluates the wall effects on particle motion and elbow erosion, emphasizing differences in erosion patterns for small particles in liquid flows under gas and liquid flow conditions. Sedrez et al. (2019) analyzed erosion in 90° elbows under liquid-dominated liquid-solid and dispersed-bubble-solid flows through experiments and CFD simulations, confirming that the maximum erosion locations predicted by CFD are near the elbow outlet, consistent with experimental data (Zahedi et al., 2017). Used CFD to simulate multiphase flows and erosion under annular flow and low liquid loading conditions, investigating particle impact characteristics and validating liquid film thickness trends (Dubey et al., 2011). Coupled discrete element modeling (DEM) with CFD to predict erosion in pipeline elbows, incorporating particle shapes and interaction factors to improve accuracy over single-particle models. Mazumder et al. (2004) proposed a mechanistic model to predict sand erosion in multiphase flows in elbows downstream of vertical pipes, considering particle impact velocities and validated by experimental data. In addition, Shi et al. (2023) integrated CFD modeling with corrosion sensor optimization to enhance corrosion monitoring effectiveness. These works fully demonstrate the effectiveness of CFD in simulating flow dynamics, liquid distribution, and erosion, applicable to various natural gas pipeline configurations involving solid particles or multiphase flows.

Despite these notable advancements, research on corrosion prediction specifically for vent pipelines in high-sulfur natural gas stations remains relatively limited. Most existing studies focus on production or transportation pipelines, with few addressing the unique characteristics of vent systems, such as high pressure, intermittent venting conditions, complex geometries (e.g., small-diameter vents at high elevations), and high H_2S concentrations. In high-sulfur environments, recent works such as (Peng et al., 2024) simulated corrosion in high-sulfur low-pressure vent pipelines based on wall liquid phase aggregation and droplet erosion, analyzing flow fields and liquid deposition to predict corrosion-prone areas with a 90% accuracy match against field data (Li et al., 2025). Assessed corrosion in medium-pressure vent pipes at high-sulfur field stations through numerical analysis of internal wall liquid phase distribution, verifying the reliability of the prediction method based on flow dynamics and H_2S distribution.

These gaps in the literature—including the lack of dedicated CFD applications for high-sulfur vent pipelines, insufficient field data validation, and the absence of quantitative associations between simulation parameters (such as liquid phase volume fraction) and corrosion severity—highlight the novelty of this study. Specifically, this research: (1) applies CFD to high-pressure vent pipelines in high-sulfur natural gas stations, a configuration rarely explored in the literature; (2) integrates CFD simulation results with on-site ultrasonic wall thickness measurements for practical validation; (3) quantitatively establishes the correlation between simulated liquid phase volume fraction and measured corrosion severity, providing a scientific basis for optimizing inspection point selection.

Based on the literature review, the objectives of this study are: (1) to use CFD to simulate gas-liquid two-phase flow, liquid accumulation, and droplet erosion in vent pipelines, identifying corrosion-sensitive areas; (2) to validate simulation results through on-site wall thickness measurements; (3) to derive quantitative correlations to improve the selection of corrosion monitoring points, thereby enhancing the safety and reliability of the station.

2 Numerical simulation

2.1 Basic physical model

2.1.1 Governing equation

The Mixture model (Equations 1–3), which is a simplified approach within the Eulerian–Eulerian framework (Manninen et al., 1996), was used in this study. In this model, both phases are treated as interpenetrating continua, but the slip velocity between phases is simplified compared with the full Eulerian-Eulerian method, making it particularly suitable for dilute gas-liquid flows.

$$\frac{\partial \rho_m}{\partial t} + \nabla \cdot (\rho_m u_m) = 0 \tag{1}$$

$$u_m = \frac{1}{\rho_m} \sum_{k=1}^{n} \alpha_k \rho_k u_k = \sum_{k=1}^{n} c_k u_k \tag{2}$$

$$\rho_m = \sum_{k=1}^{n} \alpha_k \rho_k \tag{3}$$

where ρ_m is the average density of the mixture phase, kg/m^3; ρ_k is the density of the k phase, kg/m^3; u_m is the average velocity of the

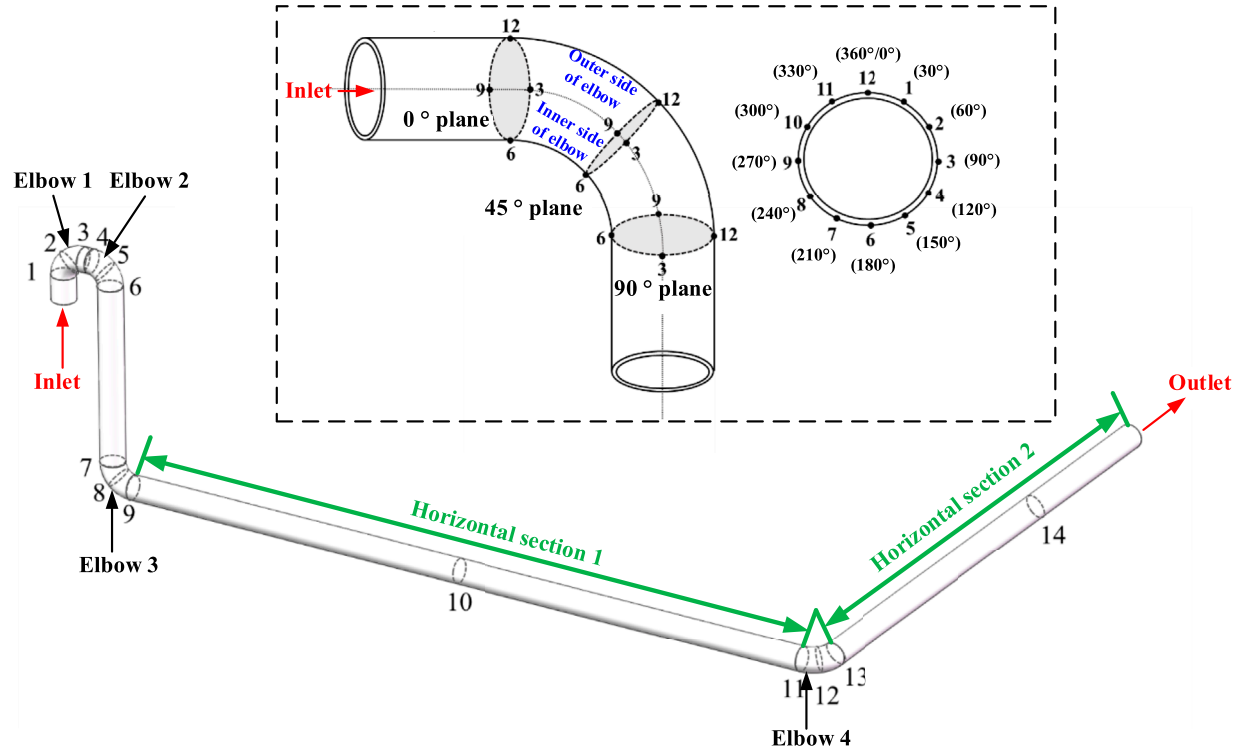

FIGURE 1
3D model of the high-pressure vent pipeline.

mixture phase, m/s; u_k is the velocity of the k phase, m/s; and α_k is the volume fraction of the k phase, %.

2.1.2 Turbulence model

The RNG k-ε model (Equations 4 – 6) (Wang and Hu, 2012) was selected in this study because it improves the prediction of swirling and recirculating flows in curved ducts compared with the standard k-ε model, while retaining numerical robustness and moderate cost. For the present high-Reynolds-number elbow flow, pilot runs showed stable convergence and physically realistic secondary-flow (Dean vortex) structures. We also screened the realizable k-ε (and SST k-ω for a subset); key distributions (velocity magnitude and liquid holdup) differed within 5%, so RNG k-ε was adopted for the full matrix. The relevant equations are as follows:

$$\rho u_i \frac{\partial k}{\partial x_i} = \frac{\partial}{\partial x_i}\left[\left(\mu + \frac{\mu_t}{\partial_k}\right)\frac{\partial k}{\partial x_i}\right] + G_k - \rho\varepsilon \tag{4}$$

$$\rho u_i \frac{\partial \varepsilon}{\partial x_i} = \frac{\partial}{\partial x_i}\left[\left(\mu + \frac{\mu_t}{\partial_k}\right)\frac{\partial \varepsilon}{\partial x_i}\right] + G_{1\varepsilon}G_k\frac{\varepsilon}{k} - G_{2\varepsilon}\rho\frac{\varepsilon^2}{k} \tag{5}$$

$$u_t = \rho C_\mu \frac{k^2}{\varepsilon} \tag{6}$$

where k is turbulent kinetic energy, kg·m·s^{-1}; ε is turbulent dissipation rate, m^2/s^3; G_k is turbulent kinetic energy generated by the average velocity gradient, kg·m·s^{-1}; μ_t is turbulent viscosity, Pa·s; RNG theoretical analysis shows that $G_{1\varepsilon}$ = 1.42, $G_{2\varepsilon}$ = 1.68, C_μ = 0.0845 (Peng et al., 2020).

2.1.3 Erosion model

The built-in Fluent liquid-droplet impingement erosion model (Liu et al., 2022) was selected in this study because it explicitly accounts for droplet diameter, impact angle, and relative velocity, all of which are dominant factors in droplet erosion under gas-carrying vent conditions, and it has been widely applied to elbows. The relevant equations (Equations 7–10) are as follows:

$$ER = \sum_{n=1}^{N} \frac{m_p C(d_p) f(\theta) u_p^{b(v)}}{A_f} \tag{7}$$

$$f(\theta) = 2.69\theta + 1.61\theta^2 - 8.84\theta^3 + 7.33\theta^4 - 1.85\theta^5 \tag{8}$$

$$C(d_p) = 1.8 \times 10^{-9} \tag{9}$$

$$b(v) = 2.6 \tag{10}$$

where N is the number of colliding particles; m_p is the mass flow rate of the particles, kg/s; $C(d_p)$ is a function of the particle diameter; $b(v)$ is a function of the relative velocity; A_f is the area of the wall calculation unit, m^2; and u_p is the velocity of the particles relative to the wall, m/s.

2.2 Numerical model

In this study, CFD numerical simulation was used to analyze the high-pressure vent pipeline at a natural gas station in Sichuan

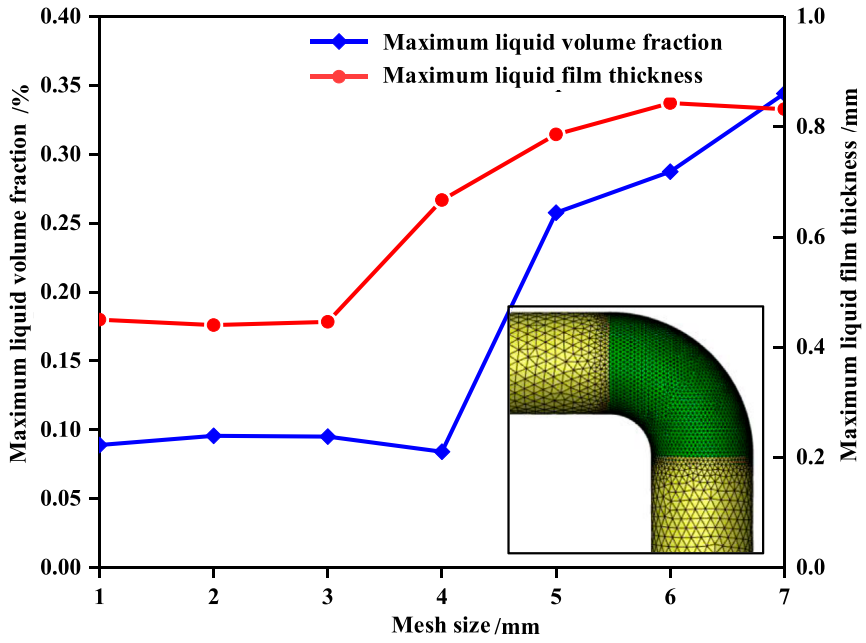

FIGURE 2
Influence of mesh size on calculation results.

Province, China, with a high sulfur content, in order to identify corrosion-sensitive areas. The three-dimensional model in Figure 1 was constructed directly from the as-built geometry measured on site. Using the field geometry enables the CFD to reproduce the real layout and boundary conditions of the high-sulfur vent pipeline, so that the simulated liquid accumulation and erosion locations are representative of the plant configuration.

The pipeline had four elbows, namely, Elbow 1, Elbow 2, Elbow 3, and Elbow 4. Each elbow was marked with three planes: the 0° plane, the 45° plane, and the 90° plane. According to the flow direction of the fluid, the fluid first passed through the 0° plane, followed by the 45° plane, and finally the 90° plane. Therefore, the 0° plane included planes 1, 4, 7, and 11; the 45° plane included planes 2, 5, 8, and 12; and the 90° plane included planes 3, 6, 7, and 13. In addition, 12 measurement points were set on each plane. The total length of the pipeline was 4,870 mm, with a nominal diameter of 80 mm. According to on-site measurements, the operating pressure of the high-pressure vent pipeline was 7 MPa, the operating temperature was 14 °C, and the densities of the gas and liquid phases were 0.83 kg/m^3 and 997.295 kg/m^3, respectively, with a liquid phase content of 0.198%.

The CFD simulations were performed using ANSYS Fluent 2022 under steady-state conditions, consistent with the station's stable operating regime. The RNG k–ε turbulence model, detailed in Section 2.1.2, was used for all cases to capture the turbulent characteristics of the gas–liquid two-phase flow in the elbows. The SIMPLE pressure–velocity coupling algorithm was adopted, while all transport equations (momentum, volume fraction, and energy) were discretized using the second-order upwind scheme to improve numerical stability and accuracy. Gradients were computed using the Green–Gauss cell-based method.

Convergence was considered achieved when the scaled residuals of all governing equations dropped below 1×10^{-5}, and the monitored outlet mass flow rate remained stable within ±0.5% over 200 iterations. To ensure the reliability of near-wall shear and liquid film predictions, the mesh near the pipe walls was refined to maintain a dimensionless wall distance of $30 < y^+ < 100$, which is appropriate for the standard wall function employed by the RNG k–ε model. A grid independence test confirmed that further mesh refinement resulted in less than 2% variation in wall shear stress and liquid phase volume fraction.

These numerical settings ensured convergence stability, near-wall resolution adequacy, and reliable reproduction of the liquid accumulation and erosion-prone regions in the high-sulfur vent pipeline.

In the numerical model, the flow velocity measured on-site (15 m/s) was set as the inlet velocity. Since the flow being simulated was viscous, the wall was chosen as a no-slip wall, meaning both the tangential and normal velocities at the wall were set to 0. To achieve more convergent results, the turbulence specification method was set to intensity and hydraulic diameter, with the turbulence intensity set to 5% and the hydraulic diameter set to 30 mm. This study aimed to identify potential high-risk regions of liquid accumulation and erosion. The maximum liquid volume fraction was used to quantify the spatial distribution and local concentration of the liquid phase at the wall, whereas the maximum liquid film thickness characterized the properties of the two-phase interfacial layer, which regulated droplet impact frequency and effective impact energy by influencing film cushioning, re-entrainment, and near-wall shear. To prevent the model mesh size from affecting the calculation results, the mesh size was gradually reduced, and the variations in the maximum liquid volume fraction and the maximum liquid film thickness along the pipe wall were analyzed to determine a reasonable mesh size.

10.3389/fmats.2025.1713051

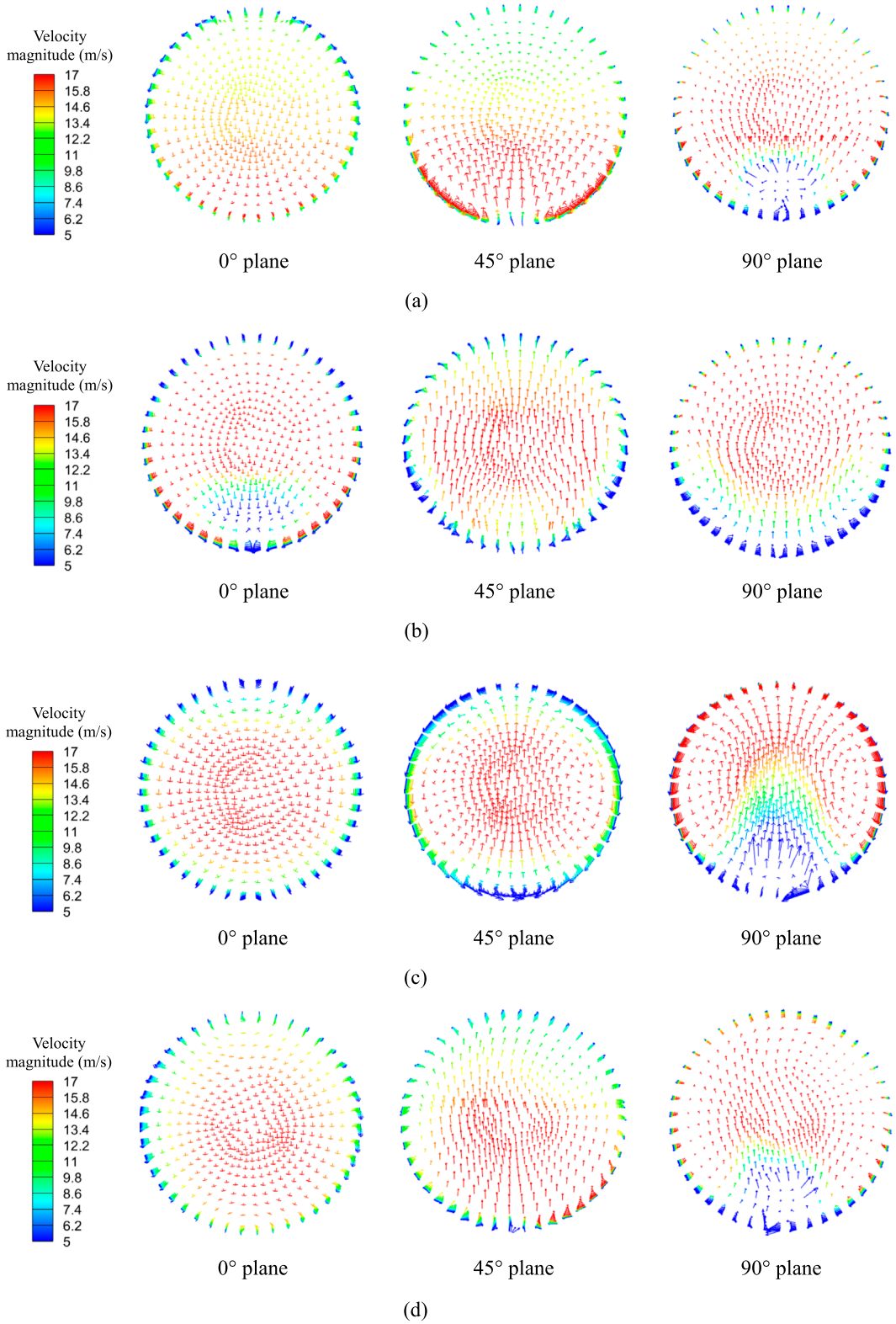

FIGURE 3
Velocity distribution of the fluid at different planes of the elbow. **(a)** Elbow 1. **(b)** Elbow 2. **(c)** Elbow 3. **(d)** Elbow four.

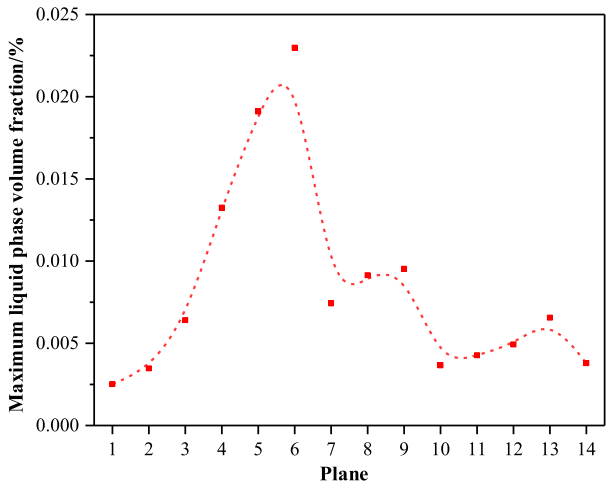

FIGURE 4
Maximum liquid phase volume fraction at different planes.

The corresponding mesh element counts for the some tested sizes were approximately 85 × 10^3 (5 mm), 200 × 10^3 (4 mm), and 450 × 10^3 (3 mm). The analysis results showed that when the mesh size was 3 mm, the maximum liquid volume fraction and the maximum liquid film thickness no longer changed significantly as the mesh size decreased, as shown in Figure 2. Therefore, a mesh size of 3 mm was chosen, with mesh refinement applied to the pipe elbows.

3 Result analysis

The analysis proceeded as follows: first, the velocity field and secondary-flow structures across the 0°, 45°, and 90° planes (Figure 3) were described; second, liquid accumulation was quantified using the maximum wall liquid volume fraction and wall film thickness (Figures 4, 5); third, droplet trajectories and erosion patterns obtained from the DPM solution were analyzed (Figures 6–8); finally, the simulated high-risk zones were compared with the on-site wall-thickness losses (Table 1), and the correlation summarized in Figure 10 was emphasized.

3.1 Internal flow field of pipeline

3.1.1 Flow fields in different planes

Figure 3 shows the velocity distribution of the fluid at different planes of the elbow. The fluid first entered Elbow one from the inlet (Figure 3a), where the flow direction changed and the maximum velocity shifted toward the outer side of the elbow. The airflow on the inner side of the elbow flowed in the opposite direction of the main gas flow, resulting in a backflow phenomenon (Li et al., 2025). When the fluid entered Elbow 2 (Figure 3b), the backflow phenomenon on the inner side of the elbow became more pronounced, and the highest velocity continued to shift toward the outer side of the elbow. The secondary flow intensity increased, and the backflow region gradually expanded. After the fluid entered Elbow 3 (Figure 3c), the backflow phenomenon slightly weakened at the 0° plane, and the highest velocity shifted toward the center axis. As the fluid passed through the other two planes of the Elbow 3, the highest velocity shifted back toward the outer side of the elbow, and the backflow phenomenon strengthened. Before entering Elbow 4, the fluid passed through a relatively long horizontal section, where the secondary flow intensity gradually decreased and the backflow phenomenon weakened. However, after entering Elbow 4 (Figure 3d), the backflow phenomenon reappeared.

Overall, Figure 3 reveals the secondary flow and backflow that govern droplet migration; the observable velocity core shift and inner-wall recirculation foreshadow the liquid accumulation trends discussed in Figures 4, 5.

3.1.2 Liquid distribution in different planes

Figure 4 shows the maximum liquid phase volume fraction at different planes of the high-pressure vent pipeline. It can be observed that the maximum liquid phase volume fraction peaked at the 90° plane (i.e., plane 6) of Elbow 2, and fluctuated the most in the continuous elbow section (i.e., planes 1–6). This was due to the severe backflow phenomenon at the continuous elbow section, where the liquid phase accumulated extensively on the outer side of the elbow under the combined effects of secondary flow and gravity. Influenced by the secondary flow formed by Elbow 2, the liquid phase volume fraction at the 0° plane (i.e., plane 7) of Elbow 3 decreased slightly. However, after entering the 45° and 90° planes (i.e., planes eight and 9) of Elbow 3, turbulence intensified, and under the effects of centrifugal force and gravity, the liquid phase re-accumulated, leading to a higher liquid phase volume fraction on the outer side of the elbow. In the horizontal sections (planes 10, 14), the fluid flow gradually stabilized, and the liquid phase accumulation was significantly alleviated compared to the elbow. In these sections, the liquid phase accumulation was mainly dominated by gravity, so the liquid phase primarily accumulated at the bottom of the pipeline.

To further clarify the liquid phase accumulation positions at each plane, the liquid phase distribution diagrams at various planes were extracted, as depicted in Figure 5. After the fluid entered Elbow 1, the liquid phase accumulated on the outer side of the elbow under the influence of gravity and centrifugal force, as illustrated in Figure 5a. Meanwhile, as the elbow angle increased, the maximum flow velocity shifted towards the outer side of the elbow, which led to the liquid phase being more likely to accumulate at the top of the elbow, as shown in Figures 5b,c. After entering Elbow 2, the fluid flowed downward. Under the effect of secondary flow, the fluid experienced a greater centrifugal force, causing part of the liquid phase to accumulate on the outer side of the 0° plane, as illustrated in Figure 5d. As the elbow angle increased, the backflow zone expanded. At this point, the direction of centrifugal force changed, and under the combined influence of gravity and centrifugal force, the liquid phase moved towards the outer side of the elbow, as observed in Figures 5e,f. Subsequently, as the fluid passed through a vertical section and the secondary flow phenomenon weakened, the liquid phase moved from the outer side of Elbow two along the wall towards the inner side of Elbow 3. Due to the weakening of the backflow phenomenon, the maximum flow velocity shifted towards the center of the pipeline, causing part of the liquid phase to accumulate on the outer side of Elbow 3, as shown in Figure 5g.

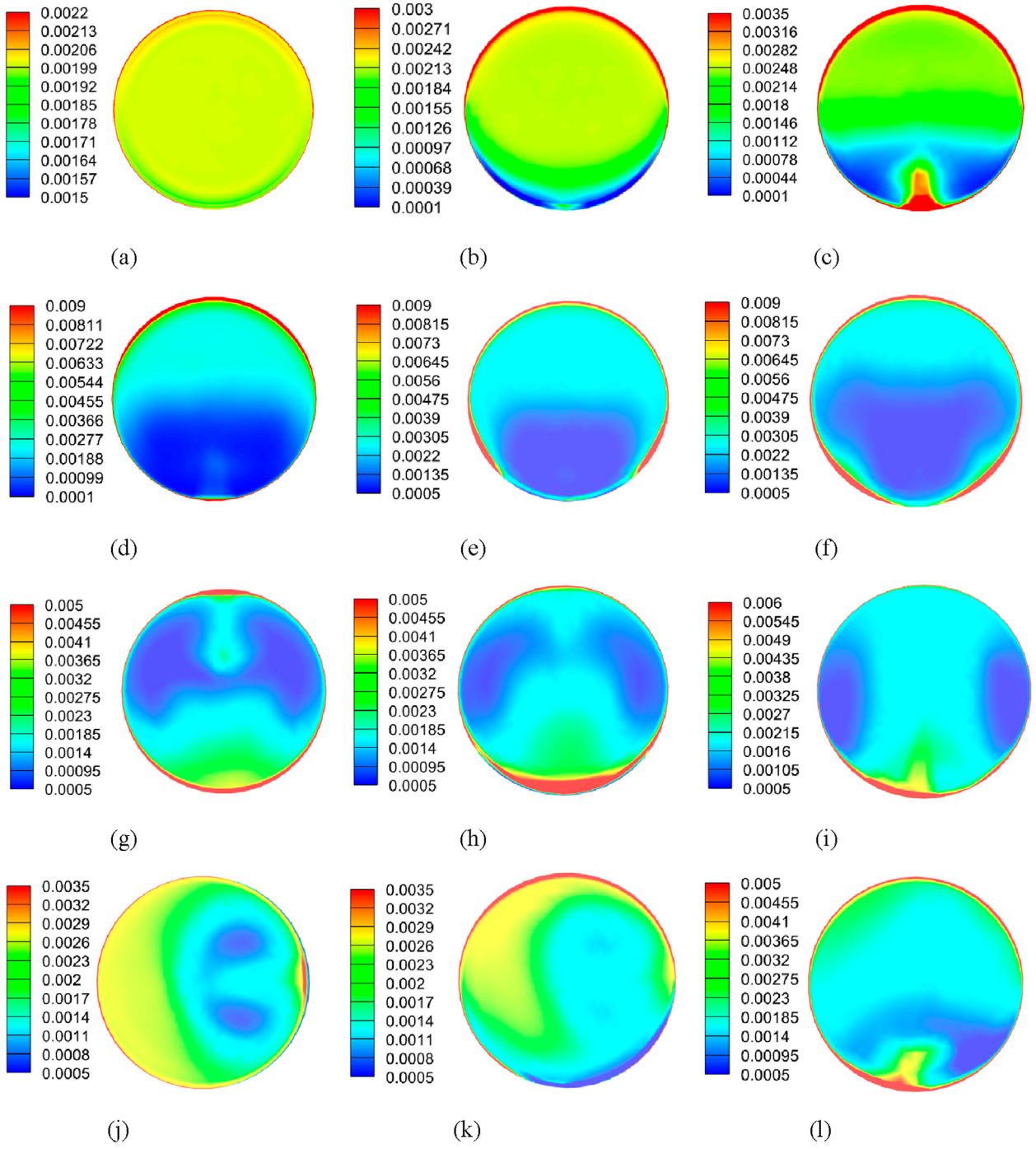

FIGURE 5
Liquid phase distribution diagrams at various planes. **(a)** plane 1. **(b)** plane 2. **(c)** plane 3. **(d)** plane 4. **(e)** plane 5. **(f)** plane 6. **(g)** plane 7. **(h)** plane 8. **(i)** plane 9. **(j)** plane 11. **(k)** plane 12. **(l)** plane 13.

As the elbow angle increased, the fluid flowed in the opposite direction, leading to more liquid phase accumulation on the outer side of Elbow 3, as depicted in Figures 5h,i. By the time the fluid reached the final elbow, the liquid phase gradually spread from the outer side of the elbow toward both sides of the inner wall, as illustrated in Figures 5j–l.

Overall, consistent with the flow features shown in Figure 3, the maximum liquid volume fraction and film thickness were enriched on the outer sides of consecutive elbows, indicating longer near-wall residence and greater droplet availability. These conditions intensified droplet impingement, as evidenced by the DPM results in Figures 6–8.

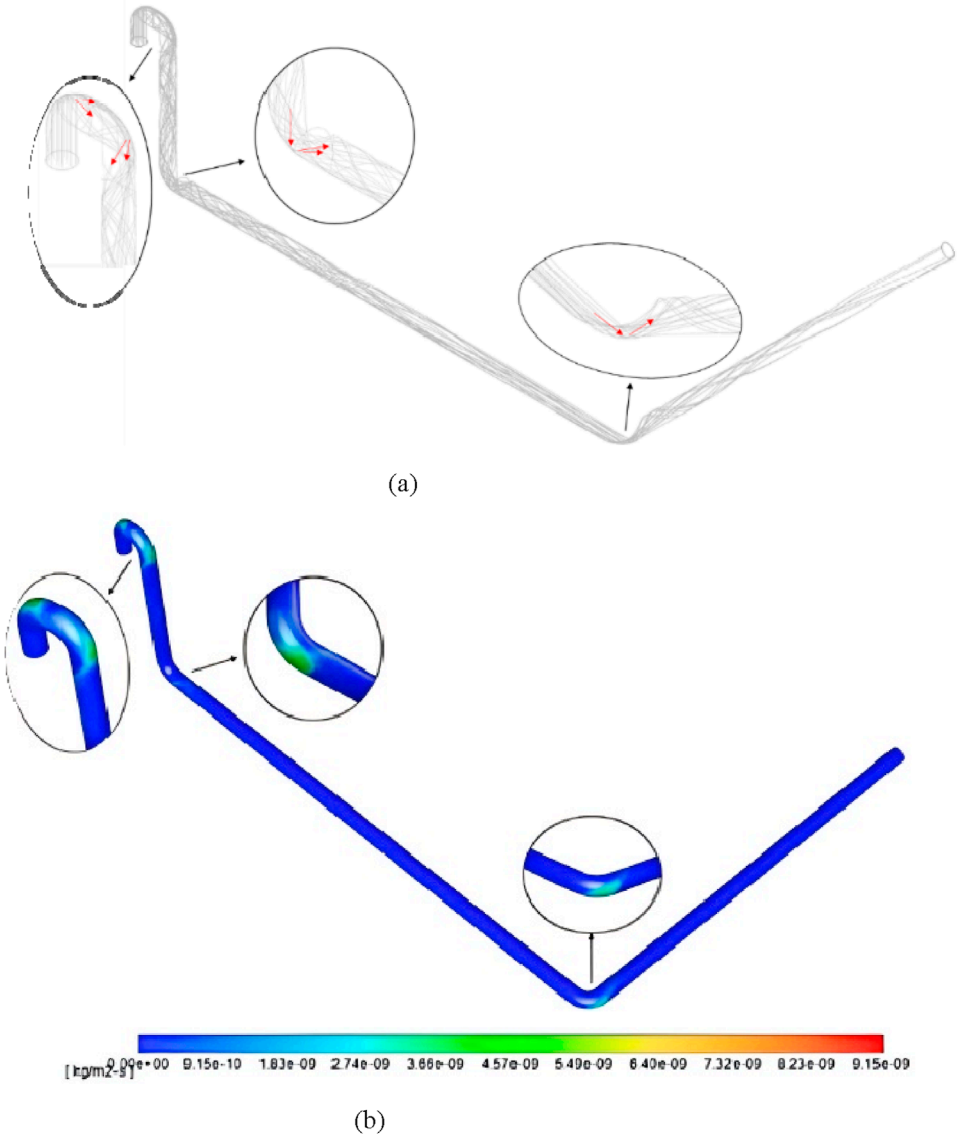

FIGURE 6
Erosion simulation. **(a)** erosion trajectory. **(b)** erosion rate distribution.

3.1.3 Elbow erosion analysis

The discrete phase model (DPM) can effectively simulate the erosion effects of liquid droplets carried by natural gas in pipelines. In this study, droplets (ρ = 1000 kg/m^3) were injected at the inlet as a surface injection with a Rosin-Rammler size distribution (mean diameter d = 50μm, spread n = 3.5, bounds 10–150 μm), and the volume concentration was set consistent with the measured liquid content (0.198%). As shown in Figure 6, the droplets, carried by the high-speed flowing natural gas, struck the inner wall of Elbow 1. Subsequently, the fluid entered Elbow 2. Under the influence of gravity and centrifugal force, the trajectories of the droplets were more concentrated, and some droplets collided, flowing along the inner wall of the elbow towards the straight pipeline section. The fluid diffused in a "V" shape in the straight pipeline section. Afterward, the diffused droplets, flowing with the airflow, struck the outer side of Elbow 3. Due to the inertia of the fluid, some droplets rebounded towards the upper part of the horizontal pipeline section, forming a more severe erosion area. This was because the diffused droplets gathered again at Elbow three and gained more energy under the influence of secondary flow. Compared with the erosion area at Elbow 1, the erosion area at Elbow three was smaller. This was because the direction of airflow changed when passing through the elbow, and some droplets were adsorbed onto the pipeline wall after impacting the elbow. As a result, the number of droplets impacting the elbow gradually decreased, leading to reduced erosion. Similarly, after the fluid entered Elbow four from the horizontal section, some droplets rebounded from the outer side of the elbow to the upper part of the next horizontal section.

Overall, the erosion rate gradually decreased from Elbow one to Elbow 4. As shown in Figures 7, 8, the circumferential distributions of erosion rate at the 45° and 90° planes provide a quantitative comparison among the four elbows. The results indicate that the

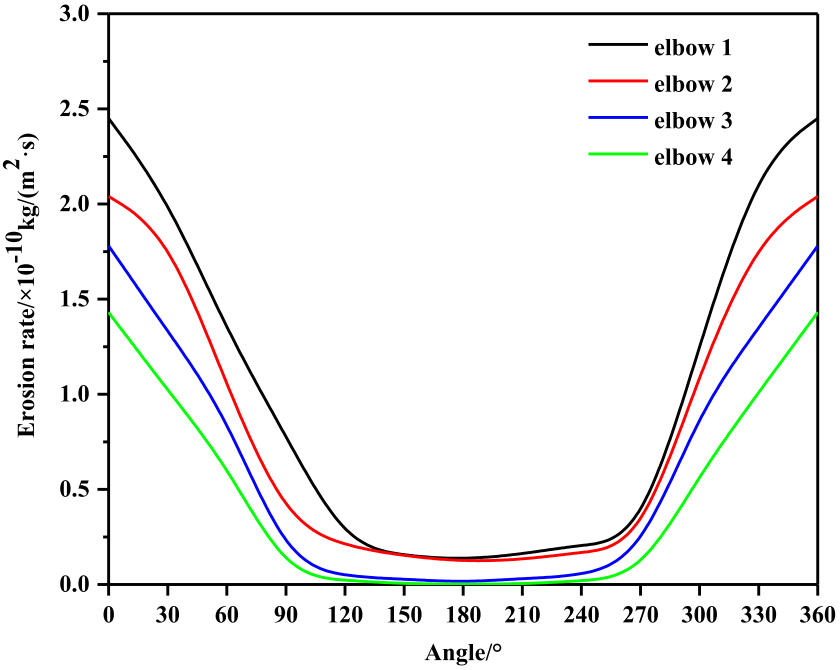

FIGURE 7
Circumferential distribution of erosion rate at 45° plane of each elbow.

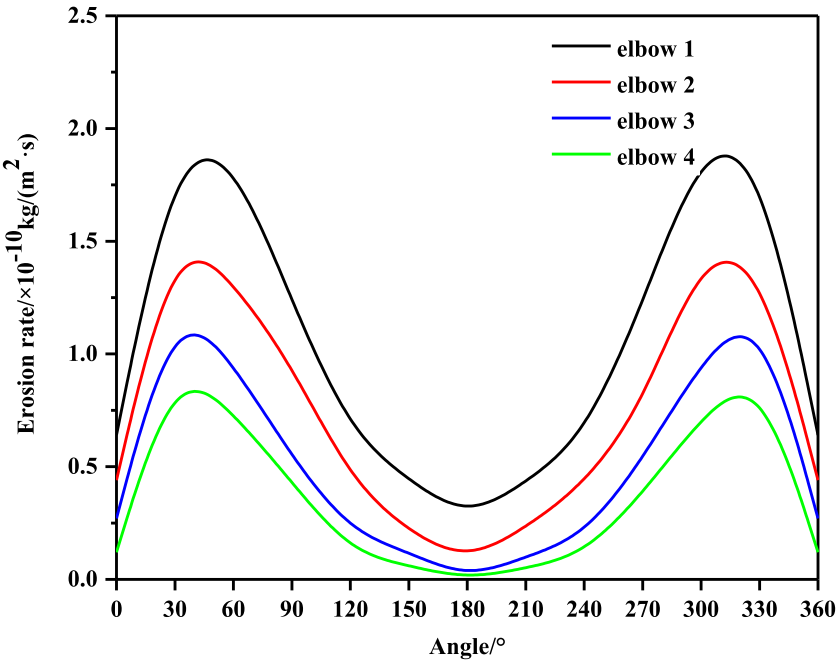

FIGURE 8
Circumferential distribution of erosion rate at 90° plane of each elbow.

outer curvature of each elbow experiences the highest erosion intensity, with Elbow one showing the most severe erosion, followed by Elbows two and 3, while Elbow four exhibits the lowest rate due to the decay of flow energy downstream. Quantitatively, the maximum erosion rate of Elbow one is approximately 70%–300% higher than that of Elbow 4. For the 45° plane, erosion was mainly concentrated in the circumferential ranges of 0°–90° and 270°–360° (Figure 7), with the maximum erosion rate occurring at the 0° circumferential

TABLE 1 Wall thickness reduction at each measurement point obtained on-site (unit: mm).

Plane	Measurement point											
	1	2	3	4	5	6	7	8	9	10	11	12
1	0.62	0.61	0.55	0.52	0.38	0.37	0.39	0.54	0.56	0.58	0.62	0.62
2	0.62	0.61	0.55	0.33	0.13	0.32	0.11	0.32	0.54	0.55	0.57	0.68
3	0.65	0.55	0.45	0.30	0.39	0.45	0.41	0.33	0.45	0.57	0.68	0.71
4	0.85	0.83	0.78	0.75	0.65	0.78	0.66	0.73	0.80	0.80	0.84	0.89
5	0.84	0.79	0.64	0.43	0.32	0.23	0.31	0.43	0.56	0.69	0.81	0.93
6	0.96	0.92	0.87	0.88	0.55	0.42	0.52	0.79	0.72	0.80	0.88	1.10
7	0.62	0.52	0.54	0.57	0.61	0.68	0.63	0.6	0.55	0.52	0.63	0.75
8	0.54	0.59	0.65	0.72	0.77	0.82	0.78	0.71	0.67	0.56	0.51	0.49
9	0.60	0.63	0.65	0.79	0.83	0.88	0.83	0.79	0.65	0.60	0.60	0.62
10	0.43	0.42	0.37	0.37	0.36	0.38	0.40	0.41	0.41	0.42	0.43	0.46
11	0.41	0.42	0.47	0.45	0.43	0.45	0.48	0.52	0.54	0.50	0.47	0.40
12	0.56	0.53	0.47	0.41	0.36	0.32	0.39	0.45	0.50	0.53	0.56	0.59
13	0.69	0.65	0.57	0.55	0.54	0.57	0.56	0.54	0.56	0.59	0.70	0.72
14	0.33	0.38	0.42	0.45	0.48	0.48	0.46	0.43	0.45	0.42	0.35	0.33

direction, which was consistent with the observed results. For the 90° plane, the erosion rate showed two peaks, located at circumferential angles of 30°–60° and 300°–330°, as shown in Figure 8. This was attributed to the "V"-shaped diffusion of droplets, which formed two peaks in the erosion rate. For the three straight pipeline sections, the vertical straight pipeline middle section and the first horizontal straight pipeline near the upper area of Elbow three experienced more severe erosion and should have been given special attention.

3.2 Relationship between liquid phase volume fraction, erosion rate, and wall thickness reduction

On-site, a high-precision ultrasonic thickness gauge (resolution ±0.01 mm) was used to measure the wall thickness of the high-pressure vent pipeline. Each plane had 12 measurement points, with the locations of the measurement points shown in Figure 1. The wall thickness reduction at each measurement point obtained on-site is shown in Table 1. Here, each point was measured 3 times and averaged. Thickness loss equals nominal baseline minus the measured value.

For Elbow 1, the liquid phase volume fraction on plane one first decreased and then increased, as shown in Figure 9a. The wall thickness reduction followed a similar pattern to the change in liquid phase volume fraction. The wall thickness reduction at measuring point 6 was 0.37 mm, while at point 12, it was 0.62 mm. For plane 2, the liquid phase volume fraction distribution and the wall thickness reduction trend were similar to those of plane 1. However, due to the effect of backflow, a peak appeared at measuring point 6 (Figure 9b), meaning that the wall thickness reduction at point 6 was greater than that at points 5 and 7. The largest wall thickness reduction in this plane occurred at point 12, reaching 0.68 mm. Additionally, the erosion rate at point 12 in this plane also reached its maximum value. For plane 3, the backflow phenomenon of the fluid became more pronounced, with some liquid flowing back between measuring points 5 and 7 (Figure 9c). Compared to plane 2, the range of the peak at measuring point 6 in plane three was expanded.

For Elbow 2, on plane 4, there was a small peak in the liquid phase volume fraction between measuring points 5 and 7, as shown in Figure 9d. On plane 5, the liquid phase volume fraction first decreased and then increased, as shown in Figure 9e. The wall thickness reduction at measuring point 12 was the largest, reaching 0.93 mm. Additionally, the erosion rate at measuring point 12 on plane five also reached its maximum. The backflow phenomenon on plane six was the most significant, as shown in Figure 9f. The backflow area was located on the inner side of the elbow, causing the liquid phase accumulated on the outer side of the elbow to gradually move toward the inner side along the circumferential pipeline wall. However, due to vortices on both sides of the plane, the liquid phase on the outer side of the elbow flowed back and accumulated again on the outer side before it could flow toward the inner side. Therefore, the largest wall thickness reduction on plane six occurred at measuring point 12, reaching 1.1 mm.

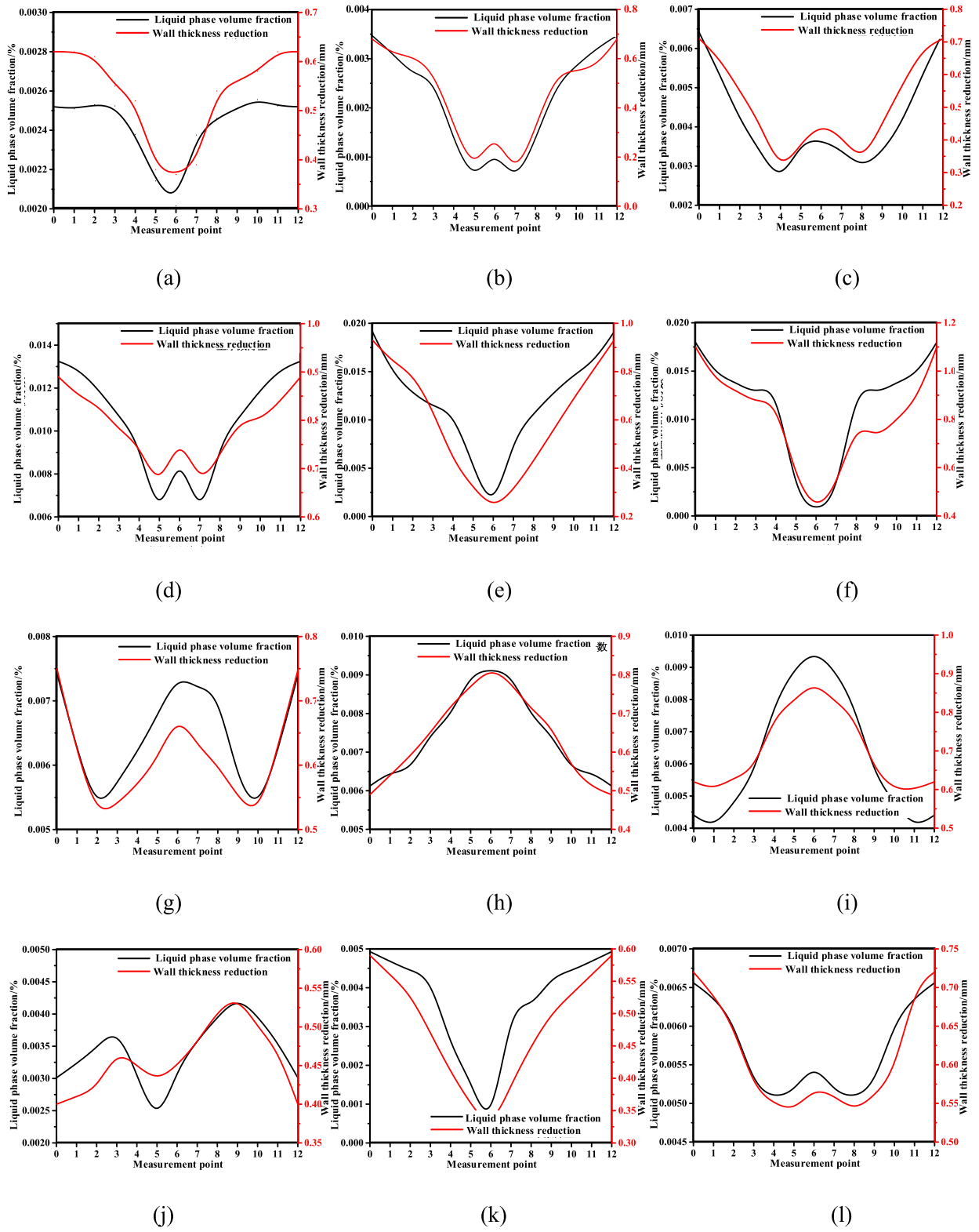

FIGURE 9
Relationship between liquid phase volume fraction and wall thickness reduction. **(a)** plane 1. **(b)** plane 2. **(c)** plane 3. **(d)** plane 4. **(e)** plane 5. **(f)** plane 6. **(g)** plane 7. **(h)** plane 8. **(i)** plane 9. **(j)** plane 11. **(k)** plane 12. **(l)** plane 13.

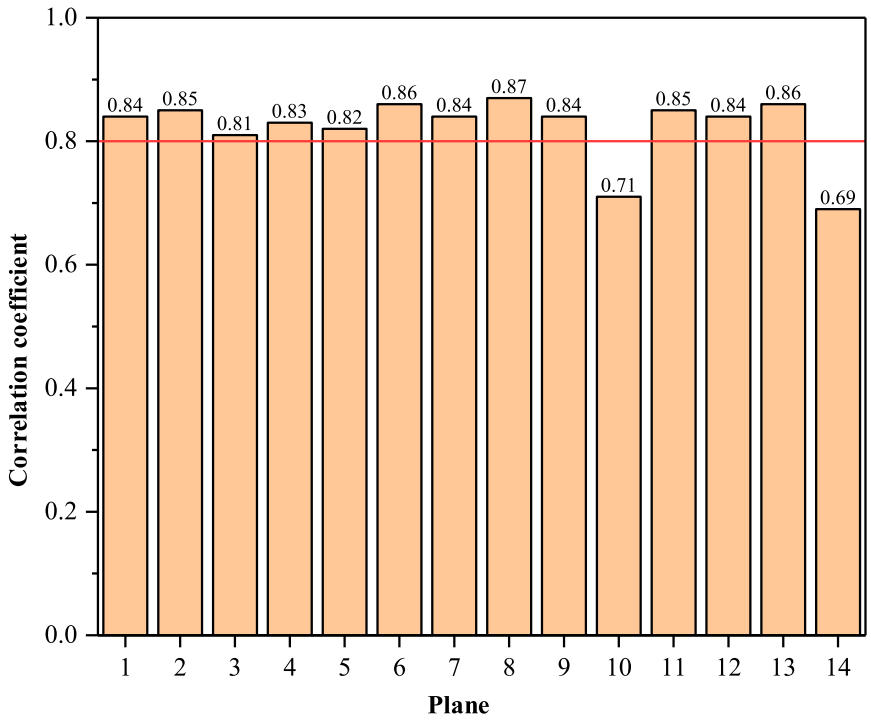

FIGURE 10
Correlation coefficient.

TABLE 2 Classification of correlation coefficient.

ρ	Correlation
0.8–1.0	Extremely strong correlation
0.6–0.8	Strong correlation
0.4–0.6	Moderate correlation
0.2–0.4	Weak correlation
0.0–0.2	Extremely weak or no correlation

For Elbow 3, on plane 7, the corrosion is mainly concentrated at points 6 and 12, as shown in Figure 9g. On plane 8, the fluid direction changed, and backflow occurred on the inner side of the elbow (Figure 9h), causing the liquid phase to accumulate inside the elbow. The wall thickness reduction at measuring point 6 was the largest, reaching 0.82 mm. On plane 9, the backflow area increased, and the vortices converged toward both sides of the plane, causing the liquid droplets on the inner side of the elbow to flow to both sides. Similarly, the largest wall thickness reduction occurred at measuring point 6, reaching 0.88 mm, as shown in Figure 9i.

For Elbow 4, on plane 11, the flow field of the straight section affected the distribution of the liquid phase, causing it to accumulate on the left side at the bottom of the pipeline. As a result, the liquid phase volume fraction and wall thickness reduction were both greatest at measuring point 9, with the wall thickness reduction reaching 0.54 mm, as shown in Figure 9j. In the straight section, the flow field had not yet fully stabilized, and the backflow effect at measuring point 3 also resulted in a larger wall thickness reduction. On plane 12, the liquid phase volume fraction was the highest at measuring point 12, and the erosion rate also reached its maximum in this plane, as shown in Figure 9k. Similarly, after the fluid entered plane 13, the liquid phase volume fraction and wall thickness reduction were both greatest at measuring point 12. Additionally, a small peak appeared at measuring point 6, as shown in Figure 9l.

To further evaluate the relationship between the liquid phase volume fraction and the wall thickness reduction, the correlation coefficient (ρ) was introduced, and its calculation formula is shown in Equation 11. If ρ approached 1, it indicated a strong correlation between the two parameters. If ρ approached 0, it indicated a weak correlation between the two parameters, as shown in Table 2.

$$\rho(X,Y) = \frac{\sum(x-\bar{x})(y-\bar{y})}{\sqrt{\sum(x-\bar{x})^2\sum(y-\bar{y})^2}} \tag{11}$$

where x and y represent the data sets, and $\bar{x}$ and $\bar{y}$ represent the mean values of the data sets.

Figure 10 shows the relationship between the liquid phase volume fraction and the wall thickness reduction. For the planes of the elbows (i.e., planes one to nine, planes 11-13), the correlation coefficient between the liquid phase volume fraction and the wall thickness reduction ranged from 0.81 to 0.87. For the straight pipelines (planes 10 and 14), it ranged from 0.69 to 0.71. In both cases, the correlation was considered strong. A linear regression between the simulated liquid phase volume

fraction and the measured wall thickness reduction was performed, yielding a determination coefficient (R^2) of 0.72, indicating strong agreement between CFD predictions and field measurements. The mean absolute percentage error (MAPE) was 8.6%, confirming the quantitative reliability of the correlation. It is worth emphasizing that wall thickness reduction results from the combined action of corrosion and erosion. A higher liquid phase volume fraction implies longer near-wall residence and greater droplet availability, thereby increasing both droplet impingement and acid exposure; accordingly, planes with higher values tend to exhibit larger thickness losses.

4 Conclusion

This study analyzed the flow fields, liquid phase volume fraction distribution, and erosion phenomena in the high-pressure vent pipelines of a high-sulfur natural gas station, combined with on-site wall thickness measurements to validate the CFD results. The main conclusions are as follows:

1. Secondary flow phenomena occurred inside the elbows, causing the liquid phase to accumulate on the outer side of the elbows due to centrifugal force. Continuous elbows exhibited more intense secondary flow, making liquid phase accumulation easier. As the fluid flow distance increased, the secondary flow intensity decreased.
2. Under the same flow rate, the four elbows experienced varying degrees of erosion. The most severe erosion occurred on the outer side of the elbow, particularly between the 45° and 90° planes, where the predicted erosion intensity and measured wall thinning were both the highest. This confirms the CFD model's effectiveness in locating potential corrosion hot spots.
3. Both liquid phase accumulation and erosion contributed to wall thickness reduction. The correlation coefficient between the simulated liquid phase volume fraction and the measured thickness reduction exceeded 0.69, demonstrating a strong positive relationship. This quantitative correlation provides a scientific basis for selecting corrosion monitoring points and optimizing inspection intervals in similar high-sulfur vent pipelines.

Overall, this study established a validated CFD-based approach for predicting corrosion-prone regions in complex vent pipeline systems. The findings can be applied to guide corrosion sensor placement and risk assessment in high-pressure natural gas facilities. Future work will focus on integrating CFD results with *in-situ* corrosion monitoring data for real-time integrity management.

Data availability statement

The original contributions presented in the study are included in the article/supplementary material, further inquiries can be directed to the corresponding author.

Author contributions

JL: Writing – original draft. JS: Writing – review and editing. LT: Writing – original draft. LZ: Writing – original draft. DD: Writing – original draft. YL: Writing – original draft. XZ: Writing – original draft.

Funding

The authors declare that no financial support was received for the research and/or publication of this article.

Conflict of interest

Authors JL, JS, and LZ were employed by PetroChina Southwest Oil and Gasfield Company.

Authors LT and DD were employed by PetroChina Southwest Oil and Gasfield Company.

The remaining authors declare that the research was conducted in the absence of any commercial or financial relationships that could be construed as a potential conflict of interest.

Generative AI statement

The authors declare that no Generative AI was used in the creation of this manuscript.

Any alternative text (alt text) provided alongside figures in this article has been generated by Frontiers with the support of artificial intelligence and reasonable efforts have been made to ensure accuracy, including review by the authors wherever possible. If you identify any issues, please contact us.

Publisher's note

References

Chen, B., Wang, Y., and He, R. (2017). Study on the prediction of corrosion location based on the water accumulation in pipeline. *China Spec. Equip. Saf.* 33 (03), 37–41. doi:10.3969/j.issn.1673-257X.2017.03.007

Darihaki, F., Zhang, J., and Vieira, R. E. (2021). The near-wall treatment for solid particle erosion calculations with CFD under gas and liquid flow conditions in elbows. *Adv. Powder Technol.* 32 (5), 1663–1676. doi:10.1016/j.apt.2021.03.020

Dubey, A., Smith, R. J. B., and Vedapuri, D. (2011). "Erosion prediction in pipeline elbow by coupling discrete element modeling (DEM) with computational fluid dynamics (CFD)," in *Nace corrosion conference*.

Fujisawa, N., Yamagata, T., Takano, S., Saito, K., Morita, R., Fujiwara, K., et al. (2015). The influence of material hardness on liquid droplet impingement erosion. *Nucl. Eng. Des.* 288, 27–34. doi:10.1016/j.nucengdes.2015.03.016

Fujisawa, N., Wada, K., and Yamagata, T. (2016). Numerical analysis on the wall-thinning rate of a bent pipe by liquid droplet impingement erosion. *Eng. Fail. Anal.* 62, 306–315. doi:10.1016/j.engfailanal.2016.01.005

Hong, B., Li, Y., Li, X., Ji, S., Yu, Y., Fan, D., et al. (2021). Numerical simulation of gas-solid two-phase erosion for elbow and tee pipe in gas field. *Energies* 14 (20), 6609. doi:10.3390/en14206609

Hu, H., and Cheng, Y. F. (2016). Modeling by computational fluid dynamics simulation of pipeline corrosion in CO_2-containing oil-water two phase flow. *J. Petroleum Sci. Eng.* 146, 134–141. doi:10.1016/j.petrol.2016.04.030

Li, J., Gong, J., Shen, J., Yang, K., Zhou, J., and Liao, Y. (2025). Corrosion prediction in medium pressure vent pipes at high sulfur field stations through numerical analysis of internal wall liquid phase distribution. *Sci. Rep.* 15 (1), 20895. doi:10.1038/s41598-025-03175-5

Liu, Y., Cui, X., and Fang, Y. (2022). Research progress on erosion damage and protective coating for aircraft engine. *China Surf. Eng.* 35 (03), 31–47. doi:10.11933/j.issn.1007-9289.20211029003

Manninen, M., Taivassalo, V., and Kallio, S. (1996). *On the mixture model for multiphase flow[R]*. Technical Research Center of Finland.

Maruschak, P., Prentkovskis, O., and Bishchak, R. (2016). Defectiveness of external and internal surfaces of the main oil and gas pipelines after long-term operation. *J. Civ. Eng. Manag.* 22 (2), 279–286. doi:10.3846/13923730.2015.1100672

Mazumder, Q. H., Shirazi, S. A., and McLaury, B. S. (2004). A mechanistic model to predict sand erosion in multiphase flow in elbows downstream of vertical pipes. *Corrosion*, 1–15. doi:10.5006/c2004-04662

Peng, S., Chen, Q., and Liu, E. (2020). The role of computational fluid dynamics tools on investigation of pathogen transmission: prevention and control. *Sci. Total Environ.* 746, 142090. doi:10.1016/j.scitotenv.2020.142090

Peng, X., Liao, Y., Gong, J., and Shen, J. (2024). Corrosion prediction in high-sulfur low-pressure vent pipelines based on wall liquid phase aggregation and droplet erosion. *Case Stud. Constr. Mater.* 20, e03253. doi:10.1016/j.cscm.2024.e03253

Sedrez, T. A., Shirazi, S. A., Rajkumar, Y. R., Sambath, K., and Subramani, H. J. (2019). Experiments and CFD simulations of erosion of a 90 elbow in liquid-dominated liquid-solid and dispersed-bubble-solid flows. *Wear* 426, 570–580. doi:10.1016/j.wear.2019.01.015

Shi, S., Jiang, B., Ludwig, S., Xu, L., Wang, H., Huang, Y., et al. (2023). Optimization for pipeline corrosion sensor placement in oil-water two-phase flow using CFD simulations and genetic algorithm. *Sensors* 23 (17), 7379. doi:10.3390/s23177379

Wang, J. Y., and Hu, X. J. (2012). "Application of RNG k-ε turbulence model on numerical simulation in vehicle external flow field applied mechanics and materials,", 170. Trans Tech Publications Ltd, 3324–3328.

Xu, S., Huang, S., Guo, D., Zhao, Y., and Song, M. (2017). Failure analysis of a carbon steel pipeline exposed to wet hydrogen sulfide environment. *Eng. Fail. Anal.* 71, 1–10. doi:10.1016/j.engfailanal.2016.11.001

Zahedi, P., Zhang, J., Arabnejad, H., McLaury, B. S., and Shirazi, S. A. (2017). CFD simulation of multiphase flows and erosion predictions under annular flow and low liquid loading conditions. *Wear* 376, 1260–1270. doi:10.1016/j.wear.2017.01.111

Zhao, W., Zou, Y., Matsuda, K., and Zou, Z. (2016). Characterization of the effect of hydrogen sulfide on the corrosion of X80 pipeline steel in saline solution. *Corros. Sci.* 102, 455–468. doi:10.1016/j.corsci.2015.10.038